Materials Research Proceedings **32** (2023) 25-40 https://doi.org/10.21741/9781644902615-3

In-situ neutron and synchrotron methods for the investigation of plastic deformation and annealing in metals

Klaus-Dieter Liss[1,a*]

[1]School of Mechanical, Materials, Mechatronic and Biomedical Engineering, Northfields Avenue, University of Wollongong, Wollongong, NSW 2522, Australia

[a]kdl@uow.edu.au, liss@kdliss.de

Keywords: Neutron Scattering, Synchrotron Radiation, Diffraction Theory, Reciprocal Space, Titanium Aluminides, High-Pressure Torsion, Phase Transformation, High-Temperature, In-Situ, Plastic Deformation, Thermo-Mechanical Processing, Dynamic Recrystallization

Abstract. Following a crash course in neutron and synchrotron diffraction standards, applications are demonstrated on selected metallic systems, comprising the atomic order in titanium aluminide intermetallics at thermal and mechanical processing. High pressure torsion processed specimens show heterogeneous structure and order. Upon heating, their nanostructure evolves revealing regimes of recovery, recrystallization and grain growth, which can be exploited for engineering designated microstructures with enhanced physical and mechanical properties. Advanced analysis of two-dimensional diffractograms by synchrotron radiation allows to distinguish microstructure transformations as well as deformation mechanisms in thermo-mechanical processing. The methods are applicable to a wide range of materials and processes allowing to speed up materials development by orders of magnitude.

Prolegomenon

Superplasticity is a phenomenon on large plastic deformation of materials occurring through many crystalline and amorphous classes of solid materials, such as metals, crystalline materials, glasses and polymers. While the phenomenon is defined by plastic strain surpassing 4, i.e., four times straining its original length in a tensile test, its micromechanical and microstructural mechanism and control are highly complex, depending on multiple internal and external parameters, such as composition, microstructure, temperature, pressure, and time. Such mechanisms in crystalline materials demand some self-healing processes counteracting work hardening, dislocation pile up, localization and involve processes as dynamic recovery, dynamic recrystallization, grain boundary gliding. In other words, diffusivity has to be high either in the bulk or though specific lower dimensional channels, such as grain boundaries and along dislocation. A study of the mechanisms ideally occurs in-situ, time-resolved and in the bulk of the material while external parameters are applied.

Neutron and high-energy synchrotron radiation are both bulk penetrating probes [1], delivered by large user-facilities of highest intensities and brilliance to allow for parametric studies, spatially and time resolved, in-situ under the applied conditions. A wide range of spectroscopic methods, imaging and diffraction are typically provided at such facilities for tackling specific aspects of the materials and their behavior. Scope of the present paper is an overview on the advanced diffraction techniques and presenting selected examples.

Neutron- and Synchrotron X-ray Diffraction

Both X-rays and neutrons are short-wavelength quantum beams with wavelengths λ of interest in the range or smaller than atomic distances in the crystalline or amorphous structure [2], subject to interferences of waves scattered by the individual atoms, presenting the effect of diffraction. By

Materials Research Proceedings **32** (2023) 25-40 https://doi.org/10.21741/9781644902615-3

the quantum-mechanical wave-particle dualism, important kinematic quantities are the wave number k, or momentum p

$$k = 2\pi / \lambda \quad ; \quad \vec{p} = \hbar \vec{k} \tag{1}$$

with $\hbar = h/2\pi$ the Planck constant, and the energy

$$E = \hbar \omega \tag{2}$$

of the particle, which are globally conserved under any transformation. An important fundamental difference between X-rays and neutrons are the dispersion relations between E and k, namely

$$E_X = \hbar c k \text{ for X-rays, and} \tag{3x}$$

$$E_n = \frac{\hbar^2 k^2}{2m} \text{ for neutrons.} \tag{3n}$$

Herein c is the speed of light and m the mass of a neutron. Values for say $k = 3.49$ Å^{-1} result in wavelength $\lambda = 1.80$ Å with energies $E_X = 6.89$ keV and $E_n = 25.3$ meV, respectively, for X-rays and neutrons. These typical values can vary in a range spanned by an order of magnitude and the selected numbers correspond to the tabulated values at neutron velocity $v = 2200$ m/s [3] and are close to typical lab X-ray energies [4].

A propagating X-ray or neutron wave contains the term

$$\psi_o = e^{i(\vec{k}\vec{x} - \omega t)} = e^{i\vec{k}\vec{x}} e^{-i\omega t} \tag{4}$$

which is the oscillating function in space x and time t. If we focus on the $k\,x$ dependence, then we are talking of diffraction, while spectroscopy is defined by studying the $\omega\,t$ behavior. We also recognize in Eq. (4) symmetry between k and x, as well as for ω and t, demonstrating that momentum space and energy space are the Fourier transforms of position and time, respectively, further called reciprocal space and frequency domain.

Under pure diffraction conditions ω is constant, $\Delta\omega = 0$, and therefore by Eqs. (2) and (3), the length k of the wavevector is conserved by

$$|\vec{k}_f| = |\vec{k}_i| \tag{5}$$

while its direction can change in a scattering processes by the momentum transfer

$$\vec{q} = \vec{k}_f - \vec{k}_i \,, \tag{6}$$

also called the scattering vector. The Laue interference condition, or also the Ewald construction state, if

$$\vec{q} = \vec{G} \text{ , especially } \vec{G} = \vec{G}_{hkl} \,, \tag{7}$$

in which $\vec{G}_{hkl}$ is a reciprocal lattice vector of a crystal, then we obtain high intensity in the reflected beam direction $\vec{k}_f$. This vectorial Laue equation, displayed in Fig. 1 is a more elegant representation

Materials Research Proceedings **32** (2023) 25-40 https://doi.org/10.21741/9781644902615-3

of the often cited Bragg equation where twice the Bragg angle θ equals the scattering angle 2θ between $\vec{k}_f$ and $\vec{k}_i$, and lattice spacing $d_{hkl} = 2\pi/G_{hkl}$.

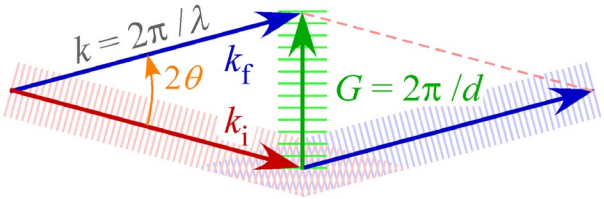

Figure 1: Laue-Bragg interference occurs when the Moiré pattern in the overlap of the incoming wave $\boldsymbol{k}_i$ *and the outgoing wave* $\boldsymbol{k}_f$ *matches the crystal lattice spacing d described by the reciprocal lattice vector* $\boldsymbol{G}$*, so that* $\boldsymbol{G} = \boldsymbol{k}_f - \boldsymbol{k}_i$*. The wavelength is* λ *and the Bragg angle* θ*, while* $k = |\boldsymbol{k}_f| = |\boldsymbol{k}_i|$.

The intensity of the reflection with Miller indices *hkl* is proporional to the structure factor, which is the Fourier transform of the crystallographic unit cell, computing

$$F_{hkl} = \sum_{\vec{\rho}_j} l_j \, e^{-i\vec{G}_{hkl}\vec{\rho}_j} \tag{8}$$

by summing scattered waves from all j atom positions $\vec{\rho}_j$ in the unit cell. The latter are weighted each by their individual scattering amplitudes l_j, expressed by the coherent bound scattering length

$$l_j = b_{c,j} \tag{9$_n$}$$

for neutrons and

$$l_j = r_e \cdot f_j(q) \cdot P(\vec{q}) \tag{9$_x$}$$

for X-rays, where r_e is the classical electron radius, i.e., the scattering length for one electron, f_j the atomic form factor, i.e., the Fourier transform of the electron distribution, and P the polarization factor, which can be set equal to $P = 1$ for small scattering angles as for high-energy X-rays.

There exist basically two orthogonal kinds of scanning reciprocal space, namely angle dispersive along the orientation of $\vec{k}_f$, i.e., along 2θ, and wavenumber dispersive by keeping 2θ fixed and varying the length of k. Some modern instruments can combine both by positioning energy dispersive detectors simultaneously at various scattering angles, making maximal usage out of the scattered radiation.

Plotting and further evaluation of diffractograms are then plotted against q or $\vec{q}$ in one to three dimenstions, representing reciprocal space in a linear coordinate system describing the sample crystal lattice rather than the machine.

Practically, conversion of the abcissa from an angular or wavenumber dispersive scale, 2θ or k, transforms via

$$q = 2\,k\,\sin(\theta) = 4\pi/\lambda\,\sin(\theta) \tag{10}$$

by fixing either k or θ, respectively. Note, in the case of energy-dispersive X-ray diffraction, Eq. (3$_x$) needs to be solved for k. For neutrons, the wavenumber dispersion is often measured by the time of flight method, where a neutron pulse of kinetic energy in Eq. (3n) is measured by the neutron time of flight τ over a flight path of length L, the diffractometer length, delivering its velocity $v = p/m$. Putting all together, the neutron time-of-flight dispersive scale transforms through

Materials Research Proceedings **32** (2023) 25-40 https://doi.org/10.21741/9781644902615-3

$$q = \frac{2m}{\hbar} sin(\theta) \frac{L}{\tau} \quad (11)$$

to linear reciprocal space, q, which is directly comparable to any angle dispersive measurement.

Bulk Penetration of Neutron- and Synchrotron Radiation

The main advantage of neutron and Röntgen radiation is their penetration into the bulk of materials while probing their structure on the atomic length scale. On top of this, immense intensities or radiation fluxes delivered by modern sources, as well as advanced instrumentation, radiation optics and detection allow for most refined and time resolved studies, enabling the recording of minute structural changes and in-situ studies.

The penetration along a linear dimension x is characterized by the attenuation into a material following an exponential law

$$\frac{I(x)}{I_0} = e^{-\mu x} \quad (12)$$

where I is the intensity, $I_0 = I(0)$ and μ the attenuation coefficient. The attenuation length is defined by the depth x_{att} at which the intensity ratio drops to e^{-1} giving $x_{att} = 1/\mu$.

Figure 2 displays the attenuation lengths for representative metals covering the light metals Al and Mg, Fe for steels, advanced structural metals Ti and Zr, precious metals Cu, Ag and Au, and heavy metals Pb and U. The X-ray curves display three ranges, namely the typical steep increase of photo-absorption at lower energies of 1~70 keV, decorated by the element characteristic absorption edges, a gentle increase between 100~1000 keV dominated by Compton scattering and finally decrease by electron-positron pair production above their threshold of 1022 keV. At the lower energies, including most common laboratory X-rays around 8 keV, photo absorption varies strongly, roughly with the third power. Passing an absorption edge removes electrons from the atom and therefore increases absorption. Compton scattering is an inelastic scattering process occurring at any electron while pair production converts photon energy into matter and anti-matter.

Neutron absorption scales with k^{-1} and is tabulated for $k = 3.49$ Å^{-1} along the scattering cross sections [3], leading to the neutron attenuation curves in the upper left corner of Fig. 2. Apart from some strong absorbing exceptions, their penetration is by orders of magnitude larger than for lab X-rays, and well larger than for high-energy X-rays.

At laboratory energies of 8 keV with $k = 4.05$ Å^{-1}, X-rays penetrate 144 μm and 74 μm into Mg and Al, 4.2 μm into Fe or steel and even less into the heavy metals Pb, Au and U. Penetrations are increased by two orders or magnitude to 37 mm, 22 mm, 3.8 mm and hundreds of micrometers, respectively, at high-energy X-rays of 100 keV ($k = 50.7$ Å^{-1}) – and those still increase significantly beyond. Neutron attenuation lengths at $k = 4.05$ Å^{-1} evaluate to 1.7 m, 0.8 m and 45 mm for Mg, Al, Fe, respectively, and 2 mm into Au.

It shall be noted that depths of a few attenuation lengths can be probed regarding the high-flux X-ray synchrotron sources, so that bulk investigations by diffraction methods are routinely feasible on most materials in the high-energy range of [80 … 200] keV and beyond. High-energy X-ray diffraction studies of penetrating 25 mm of steel have been reported in a strain scanning experiment [5] and structures of heavy element containing, few millimeter thick $EuAs_3$ been solved [6],[7].

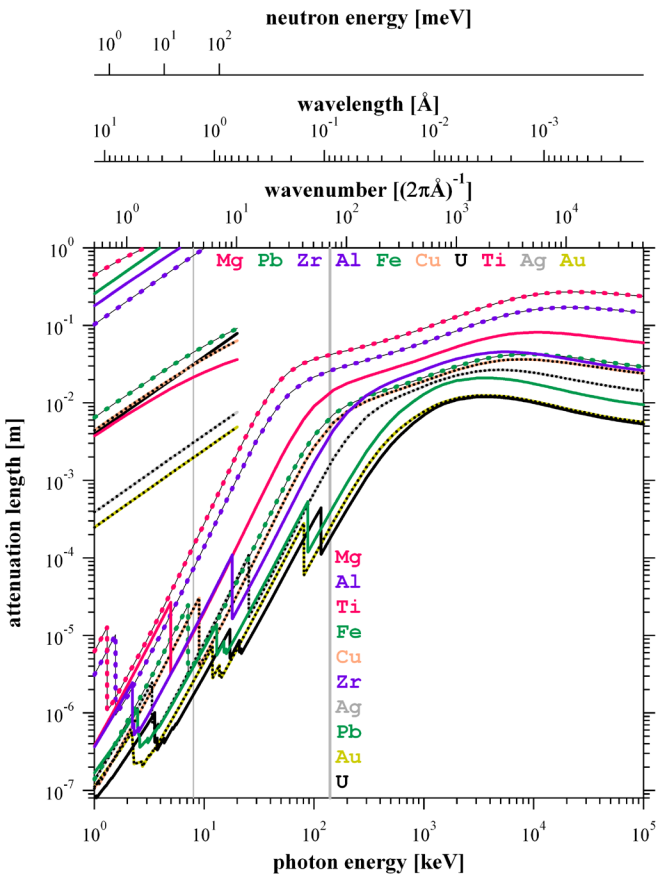

Figure 2: Attenuation lengths for typical selected elements through the periodic table. The upper left curves displayed up to 10 Å^{-1} are neutron data while the lower full-range data belong to X-rays. The colors and sequences of the element symbols correspond to their appearance from top to bottom. Cross section data taken in 1996 form the NNDC tables at NIST [8].

Usage of Neutron and Synchrotron Radiation

The applications of both kinds of quantum beams are most versatile covering all disciplines on condensed matter. Because of their deep penetration power into bulk materials, particularly high-energy synchrotron, as well as neutron radiation allow for easy sample environment, at which the beam may pass solid window materials, such as aluminum windows of a cryostat or cryo-magnet, niobium heat elements and heat shields of a high-temperature furnace, chemical reactor windows, gaskets of high-pressure cells, submerged environments, embedded sample systems, to mention but a few. Diffraction measurements range from structure determination, kinetics and dynamics of the sample system, microstructural, interfacial, and engineering applications. The salient differences for using neutrons or synchrotron radiation are compiled in Table 1.

For example, the *powder diffraction* method, as also applied to polycrystalline material demands a good statistical grain average with random orientation, in order to extract reliably peak intensities and positions, necessitating many thousand grains in the illuminated volume. As the grain size may be given by the processing of the material, neutron scattering may be advantageous over synchrotron high-energy X-ray diffraction illuminating a large gauge volume. Similar can be said for texture determination, which is the preferred crystallographic orientation averaged over a large ensemble of grains, use neutron diffraction if grains are large. On the other hand, small beam synchrotron techniques allow to probe for tiny volumes, locally, which may give information on individual or a small number of grains, even embedded in a polycrystalline matrix. When high-energy X-ray diffraction came up, *bad* grain statistics has been a problem and experimentalists spun and shifted specimens through the beam in order to get a better orientation powder average. Nowadays, we make use out of this local information, distinguished in both direct as in reciprocal space, as demonstrated in the second last chapter of this manuscript.

Materials Research Proceedings **32** (2023) 25-40 https://doi.org/10.21741/9781644902615-3

Table 1: Comparison of High-Energy X-rays with neutrons on some features.

feature	**HEX-rays**	**neutrons**
penetration	millimeters	meter
beam size / focus	micrometers - millimeters	centimeter
hydrogen sensitivity	zero	huge
light / heavy element detection	challenging to impossible	easy
magnetism	zero	sensitive
inelastic scattering	very difficult	easy
resolution	high	lower
timing	microseconds - milliseconds	seconds - hours

Another complement between the two kinds of quantum beams is the difference in scattering lengths for the various elements. For X-rays, the total scattering amplitude of the atom just increases with its atomic number *Z*, resulting that the heavy elements shine much stronger than the lighter ones. This is even dramatized as the intensity of a reflection scales with the square of the scattering length. For neutrons, the scattering length is more or less in the same order of magnitude for most of the isotopes, although unsystematic. This means, light elements can have similar scattering contribution than their heavy counterparts. Some isotopes even possess negative scattering lengths, meaning there is a 180° phase jump at those atoms in the structure. An extreme example is hydrogen, H, which scatters neutron strongest of all isotopes, unfortunately incoherently. However, the coherent scattering length of H is still strong, and in this case negative. Positive coherent scattering with much less incoherent background can be obtained through replacing the ^{1}H isotope by its heavier brother ^{2}H, also called deuterium, ^{2}D. By mixing H and D, the average scattering length can be adjusted, which is called contrast variation, allowing to match specific features in a structure (mostly in organic materials). For X-rays, however, scattering from H is practically zero, as they scatter from electrons and H usually donates its electron in a chemical compound. Thus, by comparing X-ray and neutron data, one can obtain the H-insensitive and H-sensitive part of a structure and refine the H positions. In metallurgy, H may play a role in titanium sintering, enhancing strongly the processing kinetics [9],[10].

There are other choices for neutrons prior to X-rays, which are not further emphasized here, such as sensitivity to magnetism, as the neutron itself is an elementary magnet. It allows to refine the magnetic structure and ordering in magnetic phases. Last not least, inelastic scattering is a vast field to study motions of atoms, like in diffusion, in phonons, and other collective excitations. Since thermal energies of 25 meV at room temperature are comparable with the energy of the neutron, this is the probe of choice rather than X-rays with 10^6 times larger probe energies.

An important aspect is the spatial and time resolution at which a diffractogram can be taken. This allows to follow the in situ processes in real time, while a phase transformation takes place, during the processing of a microstructure, operando while a machine is running. Selected examples will be given throughout the manuscript.

Complementary Neutron and X-ray Diffraction in Titanium Aluminides

The different atomic scattering lengths l_j between X-rays and neutrons give rise to different Laue-Bragg peak intensities through the structure factor, Eq. (8). As an example, Ti has a negative neutron scattering length, while most of the metals show positive values. For X-rays, the scattering lengths are always positive, Eq. (9_x). This feature can be applied to study the ordering in the intermetallics of the titanium-aluminide system. Figure 3 compares the diffractograms of a titanium aluminide of composition approximately Ti-45Al, comprising ordered α_2 and γ-phase. The positions of the reflections are identical on the scattering-vector scale, however, the intensities vary dramatically. The neutron scattering lengths b_c for Ti and Al are −3.438 fm and +3.449 fm,

respectively [11], while their atomic numbers *Z* are 22 and 13. The strongest X-ray peak in Fig. 3 is a superposition of the α_2-002 and γ-111 reflections. For calculating their structure factors, the scattering lengths of all atoms simply add up, which leads to ~ |22+13| = 35, a large value for X-rays, which is taken to the square for obtaining the intensity. The neutron structure factor for those reflections contains ~ |−3.438+3.449| fm = 0.011 fm, leading to a tiny intensity only, as observed in Fig. 3. On the other hand, the superstructure reflections, e.g., the first 3 neutron peaks, contain the differences of the scattering lengths, which renders them relatively small with ~ |22-13| = 9 for X-rays and huge for neutrons, by ~ |−3.438−3.449| fm = 6.887 fm, to the square, delivering the large neutron intensities, whereas X-ray peaks a tiny. Moreover, the effect of positive and negative scattering lengths can be exploited to study the crystallographic disorder of the intermetallics, when Al atoms occupy Ti sites and vice versa. Such disordered structure is described by averaging the scattering lengths on each site, which approaches the concentrations of the composition when fully disordered. Coincidentally, this value again is close to zero for neutrons, meaning, for this composition, all Bragg peaks of the disordered phase will disappear, although the material is solid and crystalline. With knowledge of the phase composition, e.g. as determined by by high-energy X-ray diffraction, the intensity of the neutron superstructure peaks gives most sensitive insight into the crystallographic order. Rather than being concentrated in Laue-Bragg interferences, the scattered intensity goes between the Bragg peaks into diffuse scattering, allowing to determine short-range order in the critical fluctuations around a phase transition [12].

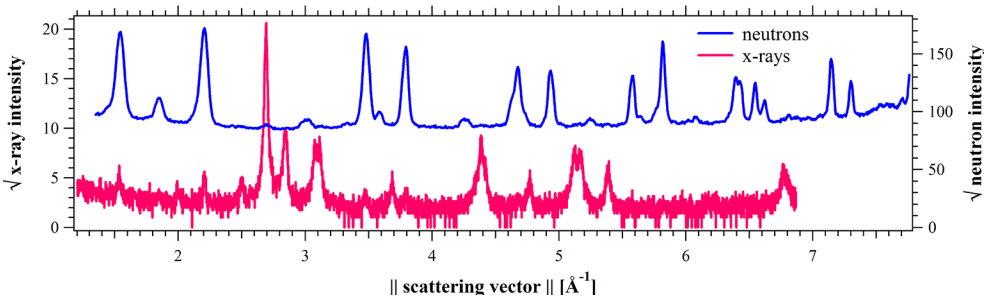

Figure 3: Comparison of neutron and X-ray diffractograms on the same scale of momentum transfer. Because of the negative scattering length of Ti, neutron peaks are strong where X-ray peaks are weak, and vice versa.

Titanium aluminides are a novel high-temperature structural material for aerospace and turbine applications. The phase composition and their crystallographic order in titanium aluminide based intermetallics is a critical parameter for their mechanical properties, influencing strongly the dislocation behavior and other plasticity aspects [13]. Quantitative thermal transformation details have been analyzed by Kabra et alii on Ti-44Al-3Mo and Ti-44Al-7Mo (in at.%) alloys [14], in which Mo may stabilize the ductile β-phase in an α+β two-phase field at high, while three ordered phases, α_2, γ and β_o exist at lower temperature, as extracted from Fig. 4. It demonstrates that the lines of all three ordered phases disappear upon heating while reappearing on cooling, revealing their individual transition temperatures and potential undercooling effects, due to nucleation. Basically, ordered, hexagonal α_2 disorders to *hcp* α in an eutectoid reaction, *ccp*-based tetragonal γ dissolves at the γ-transus, and β_o disorders to β of a ductile *bcc* structure. Similar kind of in-situ studies have been undertaken to address critical aspects in the Ti-Al-Nb phase diagram, revealing transition temperatures and phase sequences with gentle admixture of Nb by synchrotron studies [15]. The higher-Nb concentration range around the o (omicron) phase and its transformation to neighboring phases and their order clarified long-lasting discrepancies and misinterpretations in literature, particularly stating that there is only one independent kind of o phase while others can be understood as a continuous disorder transition, thriving to well-known α or α_2 in its asymptotic

limit [16]. Moreover, ordered β_o phase plays a role, which disorders again at high temperature to β. Pioneering in-situ X-ray diffraction studies of the Ti-Al system go back to Shull et alii in 1990 [17], solving part of the binary phase diagram. Although an earlier, unpublished in-situ neutron work has been cited therein, only the more challenging X-ray experiment could solve e.g. the eutectoid temperature at which α_2 disorders to α and the region at which α-phase is stable. Further clarification of phase diagrams and adjustments of databases are based on in-situ studies by Chladil et alii [18],[15]. Yeoh et alii [19] undertook the first comprehensive, synchrotron high-energy X-ray analysis connecting crystallographic order to lattice parameters, which later has been more quantified by Li et. alii [20], including effects under high hydrostatic pressure. The latter, is another physical parameter to address phase changes and stabilize the ductile β-phase under hydrostatic pressure for a potential processing window, while it disappears under operating conditions, keeping the material better creep resistant, as studied by energy-dispersive synchrotron X-ray diffraction with conditions up to 9.6 GPa and1668 K [21]. Those in-situ high-pressure experiments not only determine pressure-induced phase transformations but also indicate how a counterintuitive transformation compromising volume increase and ordering energy modify the equation of state.

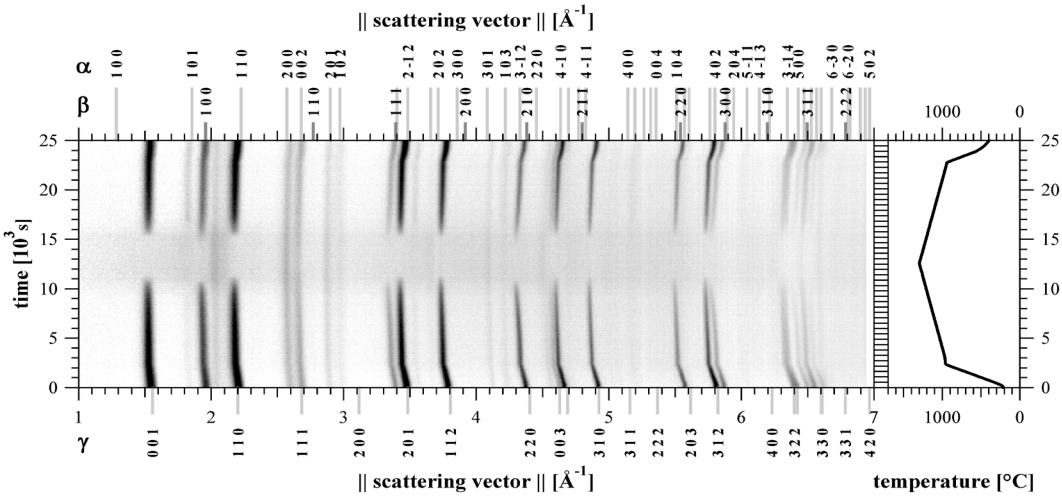

Figure 4: In-situ neutron scattering from Ti-44Al-3Mo (left) as a function of temperature (right) and time. Reproduced from Kabra et. alii [14].

Materials After Severe Plastic Deformation

Bulk nano-structured materials in metastable and heterogeneous states can be achieved by severe plastic deformation. They expose enhanced mechanical and strongly altered physical properties. For example, CoCrFeNi high entropy alloys processed by high-pressure torsion have been studied increasing Vickers hardness from 160 to 525 [22], while drastically changing ferromagnetic response to spin-clustering resulting in superparamagnetic or spinglass behavior with even inverted hysteresis [23]. Important aspects in characterizing and understanding those materials are both local volume probes for assessing heterogeneity and temperature dependent studies for revealing phase and microstructural changes.

Materials Research Proceedings **32** (2023) 25-40 https://doi.org/10.21741/9781644902615-3

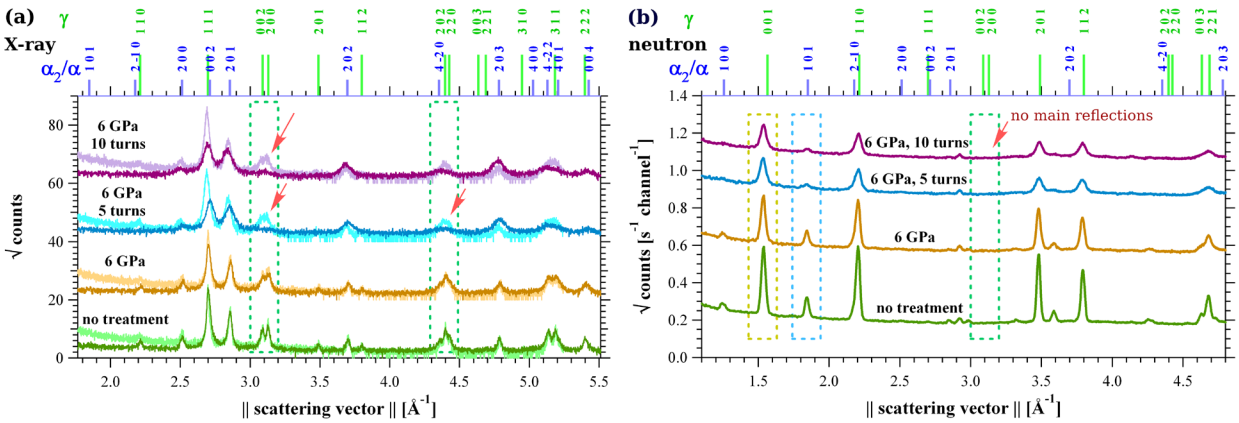

Figure 5: Lab X-ray diffraction (a) and neutron diffraction (b) of titanium aluminide Ti-45Al-7.5Nb as-received and processed by high-pressure-torsion under 6 GPa and given number of turns. The darker and lighter superimposed X-ray lines are taken at the specimen surface and mid-section layer of the disk, respectively, revealing strong heterogeneity, particular visible at the arrows. Bulk-integrated neutron diffractograms reveal decrease in intensity due to crystallographic disorder. Note the different scale ranges on the abcissa. Reproduced form Li et alii [26].

A comprehensive table has been published by Kawasaki et alii, listing both neutron and synchrotron studies on specimens after severe plastic deformation and their conditions of investigation [24]. An early study combining both synchrotron and neutron diffraction on high-pressure torsion processed material has been undertaken on a twinning-induced-plasticity steel, revealing the local and global stress induced martensitic transformation from α-Fe to ε-Fe phase, retained in the ultrafine-grained microstructure, alongside a texture analysis [25]. Titanium aluminides have been extensively investigated after high pressure torsion. Figure 5 compares laboratory Cu-K_α X-ray and neutron diffractograms by Li et alii [26]. Because X-rays around 8 keV penetrate only a few tens of micrometers, only surface-near regions are probed, first at the surface of the processed disk and then after grinding off the specimen to its mid-section. First of all, significant peak broadening can be recognized with increasing numbers of turns, i.e. shear strain, which is related to size-strain broadening as the grain size reduces and the microstrain, which is the stress-induced strain gradient between the grains of the microstructure, increases. Those X-ray data reveal that the microstructural and phase transformation at the surface is significantly different than in the mid-section, as seen e.g. at the γ-002/220 reflection pair. Upon high-pressure torsion, these peaks not only merge but almost disappear. The splitting of this couple stems from the tetragonal distortion, or the other way round, their merging reveals disorder by random anti-site occupation of Ti and Al, driving the structure to the *ccp* lattice. Such atomic disorder is valuably expressed in the neutron diffractograms by decrease of the strong superstructure reflections of both phases γ and α_2, in a similar way as discussed on the thermal driven phase transformation in Figs. 3 and 4. As the γ-phase exposes the highest ordering energy of all possible *ccp* and *hcp* based configurations [27], it rather transforms to α / α_2 and shrinks in amount. The latter has been observed already under hydrostatic pressure alone [21], while the large applied shear strain under high-pressure torsion leads to much larger disorder. Altogether, this X-ray and neutron combined study distinguishes local and global structural evolution, revealing that there exist higher plastically strained zones in the surface-near region of a high-pressure torsion specimen than in the bulk. Further inhomogeneities and their thermal evolution have been imaged by laser scanning confocal microscopy by Kawasaki et alii on high-entropy alloy specimens [24].

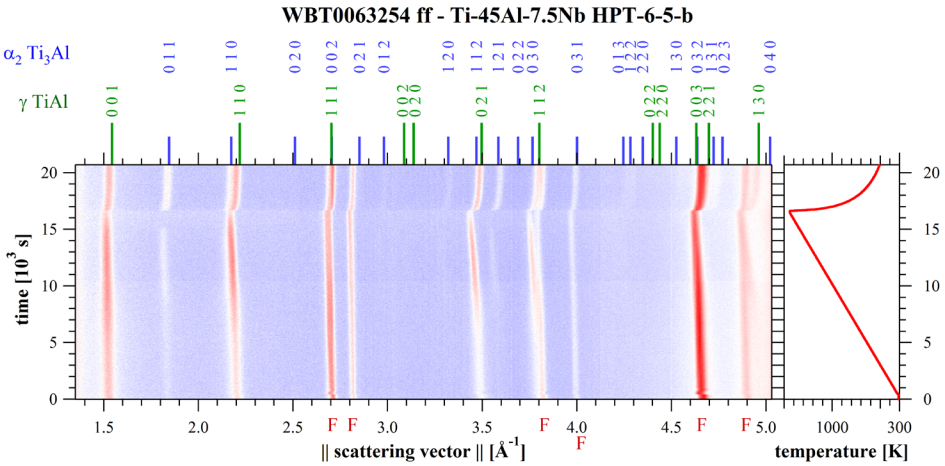

Figure 6: In-situ heating of the high-pressure torsion processed titanium aluminde under neutron diffraction from Wombat (left) undergoing a heating-cooling cycle (right). Reproduced form [28].

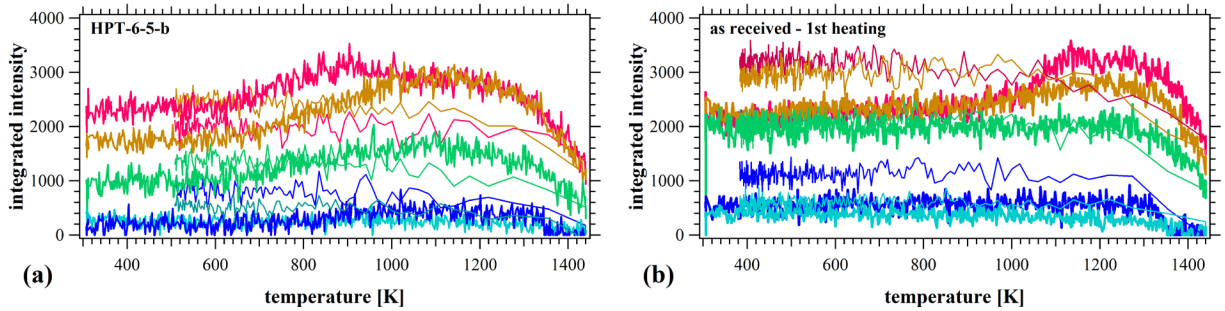

Figure 7: Extracted peak intensities from Fig. 6 on the high-pressure torsion processed (left) and as-received material (right). γ-001 (red), γ-110 (orange), γ-021 (green), α_2-011 (dark blue) and α_2-121 (light blue). Reproduced from [28].

Thermal stability and microstructural evolution of such high-pressure torsion processed specimens can be investigated by in-situ diffraction upon a heating ramp. Such neutron diffraction data is displayed in Fig. 6 showing various features: First, there are peak shifts to smaller values upon heating, due to thermal expansion of the lattice, revealing thermal expansion coefficients for the given material. Secondly, there are peak intensity and peak profile evolutions due to microstructural transformations. The salient observation in the present study, as displayed in Fig. 7a, are an intensity increase setting-in at 660 K, a relative low temperature, due to the reinstatement of crystallographic order, well before the equilibrium transformations become remarkable at about 1000 K in Fig b. As shown in the original manuscript [28], this recovery of order is consistent with afore-mentioned lattice parameter trends between fully disordered, hypothetical *ccp* and the ordered tetragonal γ-TiAl phase.

Further in-situ neutron diffraction investigations on high-pressure torsion processed CoCrFeNi high-entropy alloys are reported by Kawasaki et alii in this same journal issue [29], based on work by Liu et alii [30], which is not further reproduced here. The study employs high-resolution time-of-flight acquisition at the iMateria beamline [31] at the Materials and Life Science experimental facility [32] of the J-PARC neutron spallation source [33]. By single-peak fitting, parameters like peak positions, peak widths and integrated intensities are extracted and evaluated as a function of temperature. A minute evaluation of lattice parameters not only reveals thermal expansion and segregation of the elements, but furthermore, lattice widening due to a high concentration of vacancies has been observed. At high temperatures, these supersaturated defects recombine in a regime of recovery, followed by a sharp onset of recrystallization at which the peak widths shrink

drastically, and grains grow. As a conventional Williamson-Hall analysis, plotting peak width against peak location behaves unsystematic, the modified Williamson Hall method taking into account the anisotropic strain fields around dislocations, has been applied for obtaining reliable values of dislocation densities [30]. Very similar studies have been reported by the same group [34] on high-pressure torsion processed stainless steel. Both materials show consistently equivalent microstructural behavior on heating, correlating the different temperature regimes with hardness after annealing, revealing that hardness reaches a maximum after recovery, just before recrystallization. Such data is most valuable for designing microstructures and thus mechanical properties through severe plastic deformation and well controlled subsequent annealing. As an outlook, such microstructural design based on in-situ diffraction studies establishes a wide playground for engineering their physical properties, as the aforementioned change in magnetic response [23].

Thermo-Mechanical Processing in a Synchrotron Beam

In previous chapters we have treated the importance of grain size for accurate *powder diffraction* averaging in polycrystalline materials, which is essential for crystallographic structure determination, strain analysis, and texture acquisition. Figure 8 shows a couple of high-energy diffraction images of the same specimen of Ti-45Al-10Nb, before and after undergoing a heating-cooling cycle. It is eye-striking that the smooth continuous rings have evolved into spotty patterns, each intensity dot representing a reflection from a particular crystallite. Apart from some oxide layer (fine rings), the bulk phase composition is qualitatively similar, while certain features can be recognized in the spotty pattern: (i) intensities are concentrated in 6 regions, representing texture, which is inherited from the as-produced material. (ii) the intensity grouping across different rings reveals orientation correlations, such as Burgers, Potters and Blackburn correlations between the various phases, as well as domain orientation correlations in the γ-phase. Details have been elaborated in the pioneering works in 2006 [35].

Moreover, such rich data can be acquired during physical thermo-mechanical simulation under plastic deformation at high temperature. Azimuth-time plots have been introduced by reproducing the intensity distribution of selected reflections along a straight line, the abscissa, while streaking time along the ordinate of a two-dimensional plot [36],[37], resumed and expanded in a classical paper [38]. Results of a Ti-43.5Al-4Nb-1Mo-0.1B titanium alloy undergoing heating to 1573 K for plastic deformation are presented in Fig. 9, showing the azimuth-time plots of a selected reflection of each phase, α-101 and β-200, published by Liss et alii in 2009 [39]. The inclined, elongated streaks on α-101 prove for a grain rotation around the incoming beam axis, while their azimuthal broadening is a signature of subgrain formation. Gentle fluctuations and narrowing of the timelines witness of recovery; when in competition with the broadening, dynamic recovery; and the appearance of new lines dynamic recrystallization. The time lines seen on β-200 are very short temporally, basically dots on the graph, revealing a highly fluctuating almost random orientation distribution, which is a continuous creation and disappearance of grains, in other words, dynamic recrystallization. This data showed for the first time in-situ the deformation mechanisms at such high temperature, in real time, in two co-existing phases, proving the high formability in the α+β phase field, at which the dynamic recrystallizing β-phase takes most of the plastic strain, being the grease of the system.

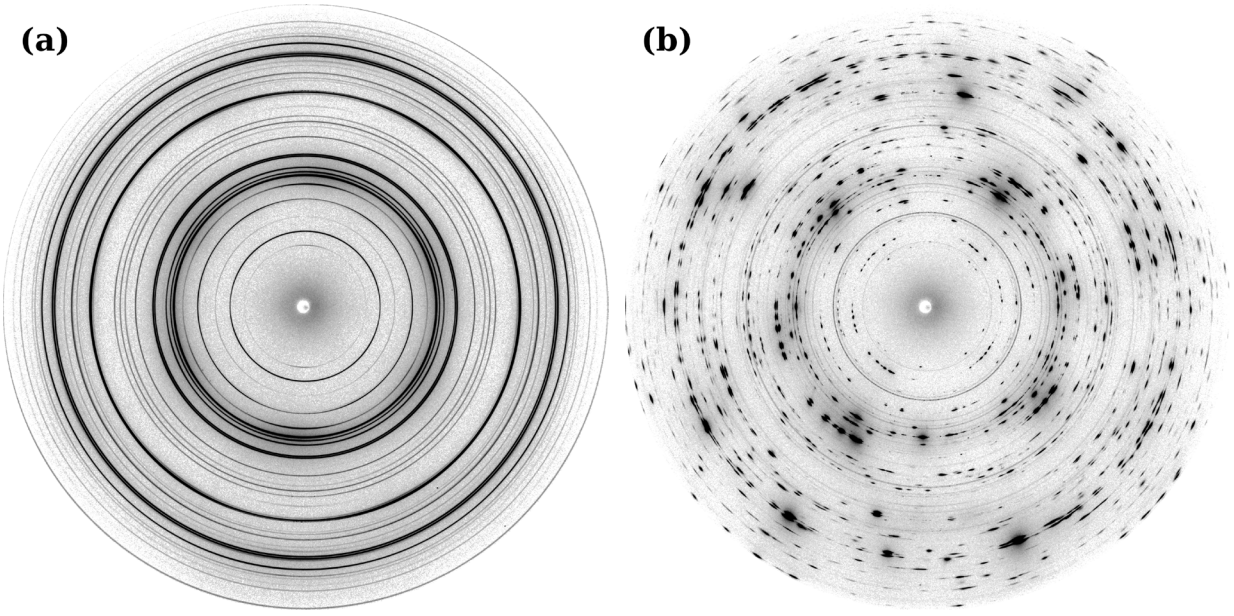

Figure 8: High-energy synchrotron X-ray diffraction from Ti-45Al-10Nb before and after heating into the high-temperature α+β-phase regime. A fine microstructure has evolved into coarse (lamellar) grains.

Extensive examples have been published by the authors describing in detail the interpretation of diffraction phenomena as well as the sample systems on Cu, Zr alloys, Mg alloys, and twinning induced plasticity steels [38],[40],[41]. A study on magnesium alloys shows the transition from extension twinning as a plastic deformation mechanism to the activation of different slip systems, resulting in different textures. Moreover, fluctuating grain orientations at static high temperatures have been observed giving raise to ongoing investigations on abnormal grain growth.

Compendium

Neutron and high-energy synchrotron radiation are most powerful tools for the investigation of bulk materials, particularly in-situ, in real time or spatially resolved. Despite the different character of radiation, individual dispersion relations and various detection and scanning methods, transformation of data into linear reciprocal space units makes them directly comparable, which can be extended to other kinds of radiation, such as electron, light and phonon scattering.

Applications in the field of metals are vast and only a few examples can be given in this limited space, selecting titanium aluminides as a primary example. Therein, negative and positive scattering lengths of neutrons versus positive ones for X-rays allow uniquely to separate crystallographic order and disorder from other effects, such as phase composition upon a transformation. An important field of application are ultra-fine grained materials obtained by severe plastic deformation, especially high-pressure torsion. Combined X-ray and neutron studies reveal different states of disorder in surface-near and deep bulk layers, testifying a high degree of heterogeneity. High-temperature studies of such specimens reveal recovery, recrystallization and grain growth regimes, allowing to micro-tune and engineer the nanostructure for increased mechanical and physical properties.

Novel methods making usage out of spotty diffraction rings can reveal a universe of complementary information, such as grain orientation correlations, transitions between them, thermally activated microstructure evolution, and during high-temperature plastic deformation. Diffraction allows to focus on a selected phase in a multi-phase material, in parallel to the others, revealing deformation by slip, dynamic recovery and dynamic recrystallization.

The methods are still in their infancy. Ongoing work actually focuses on the investigation of nanostructures with microbeams to reveal similar micostructural evolution. More comprehensive studies allow to follow grain orientations in their two dimension, revealing full orientation rearrangements, which are relevant for grain boundary rearrangements, such as in abnormal grain growth and superplasticity.

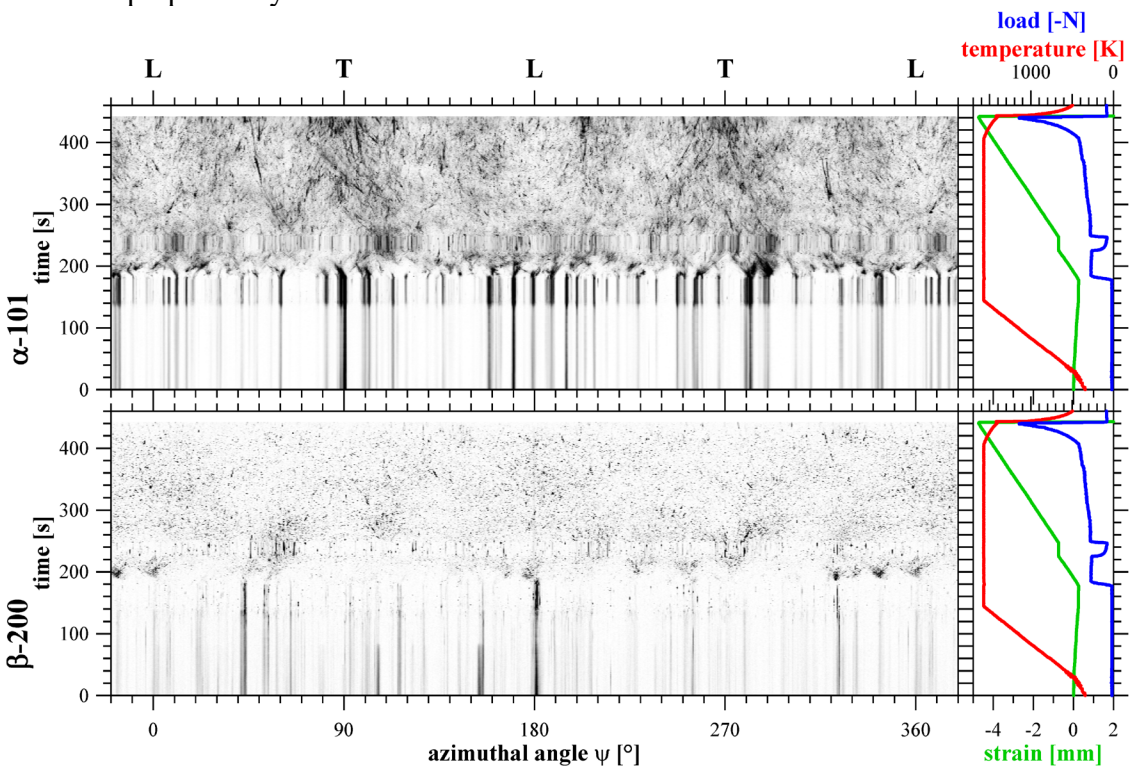

Figure 9: Azimuth-time plots of co-existing α and β phase in Ti-43.5Al-4Nb-1Mo-0.1B showing different reorientation behavior. While α deforms by crystallographic slip, some recovery and very sluggish recrystallization, the high-frequency fluctuations in the β phase reveal dynamic recrystallization. Reproduced base on [39].

Acknowledgments

The author likes to acknowledge the collaborators on the cited papers, in particular the groups around Prof. Rian Dippenaar, University of Wollongong, Prof. Megumi Kawasaki, Oregon State University, and Prof. Helmut Clemens, Montan Universität Leoben. I appeciate the many beamtimes, especially for the displayed data. At the Australian Nuclear Science and Technology Organisation ANSTO we used the WOMBAT diffractometer under proposal numbers P333 for Fig. 3, DB6022 for Fig. 4b, P6229 for Figs. 6 and 7, and time for Fig. 3. The beamline ID15B at the European Synchrotron Radiation Facility ESRF has been used for access to high-energy X-rays under proposal numbers MA-77 for Fig. 8 and MA-736 for Fig. 9.

References

[1] Liss, K.-D.; Bartels, A.; Schreyer, A.; Clemens, H. High-Energy X-Rays: A Tool for Advanced Bulk Investigations in Materials Science and Physics. *Textures Microstruct.* **2003**, *35*, 219–252. https://doi.org/10.1080/07303300310001634952

[2] Liss, K.-D. Quantum Beam Science—Applications to Probe or Influence Matter and Materials. *Quantum Beam Sci.* **2017**, *1*, 1. https://doi.org/10.3390/qubs1010001.

[3] Sears, V.F. Scattering Lengths for Neutrons. In *International Tables for Crystallography*; Vol. C, Sec. 4.4.4, pp. 444–454.

[4] Thompson, A.; Lindau, I.; Attwood, D.; Liu, Y.; Gullikson, E.; Pianetta, P.; Howells, M.; Robinson, A.; Kim, K.-J.; Scofield, J.; et al. *X-Ray Data Booklet*; 3rd Edition.; Lawrence Berkeley National Laboratory: Berkeley, 2009;

[5] Steuwer, A.; Santisteban, J.R.; Turski, M.; Withers, P.J.; Buslaps, T. High-Resolution Strain Mapping in Bulk Samples Using Full-Profile Analysis of Energy Dispersive Synchrotron X-Ray Diffraction Data. *Nucl. Instrum. Methods Phys. Res. Sect. B Beam Interact. Mater. At.* **2005**, *238*, 200–204. https://doi.org/10.1016/j.nimb.2005.06.049

[6] Tapan Chatterji; Liss, K.-D.; Tschentscher, T. Anomalous Thermal Expansion Due to Magnetism in EuAs3 and MnS2. In *ESRF Highlights 1996/1997*; 1997; p. 19.

[7] Chatterji, T.; Liss, K.D.; Tschentscher, T.; Janossy, B.; Strempfer, J.; Bruckel, T. High-Energy Non-Resonant X-Ray Magnetic Scattering from EuAS(3). *Solid State Commun.* **2004**, *131*, 713–717. https://doi.org/10.1016/j.ssc.2004.06.026

[8] Hubbell, J.H.; Seltzer, S.M. Tables of X-Ray Mass Attenuation Coefficients and Mass Energy-Absorption Coefficients 1 KeV to 20 MeV for Elements Z = 1 to 92 and 48 Additional Substances of Dosimetric Interest. *NIST* **1995**.

[9] Chen, G.; Liss, K.D.; Auchterlonie, G.; Tang, H.; Cao, P. Dehydrogenation and Sintering of TiH2: An In Situ Study. *Metall. Mater. Trans. A* **2017**, 1–11. https://doi.org/10.1007/s11661-017-4043-8.

[10] Liss, K.-D.; Whitfield, R.E.; Xu, W.; Buslaps, T.; Yeoh, L.A.; Wu, X.; Zhang, D.; Xia, K. In Situ Synchrotron High-Energy X-Ray Diffraction Analysis on Phase Transformations in Ti-Al Alloys Processed by Equal-Channel Angular Pressing. *J. Synchrotron Radiat.* **2009**, *16*, 825–834. https://doi.org/10.1107/S090904950903711X

[11] Sears, V.F. Neutron Scattering Lengths and Cross Sections. *Neutron News* **1992**, *3*, 26–37. https://doi.org/10.1080/10448639208218770

[12] Li, X.; Bhattacharyya, D.; Jin, H.; Reid, M.; Dippenaar, R.; Yang, R.; Liss, K.-D. In-Situ Studies of TiAl Polysynthetically Twinned Crystals: Critical Fluctuations and Microstructural Evolution. *J. Alloys Compd.* **2019**, 152454. https://doi.org/10.1016/j.jallcom.2019.152454

[13] Shechtman, D.; Blackburn, M.J.; Lipsitt, H.A. The Plastic Deformation of TiAl. *Metall. Trans.* **1974**, *5*, 1373–1381. https://doi.org/10.1007/BF02646623

[14] Kabra, S.; Yan, K.; Mayer, S.; Schmoelzer, T.; Reid, M.; Dippenaar, R.; Clemens, H.; Liss, K.-D. Phase Transition and Ordering Behavior of Ternary Ti-Al-Mo Alloys Using in-Situ Neutron Diffraction. *Int. J. Mater. Res.* **2011**, *102*, 697–702. https://doi.org/10.3139/146.110528

[15] Chladil, H.F.; Clemens, H.; Zickler, G.A.; Takeyama, M.; Kozeschnik, E.; Bartels, A.; Buslaps, T.; Gerling, R.; Kremmer, S.; Yeoh, L.; et al. Experimental Studies and Thermodynamic Simulation of Phase Transformations in High Nb Containing Gamma-TiAl Based Alloys. *Int. J. Mater. Res.* **2007**, *98*, 1131–1137. https://doi.org/10.3139/146.101569

[16] Xu, S.; Reid, M.; Lin, J.; Liang, Y.; Yang, L.; Zhang, J.; Liss, K.-D. The Crystal Structure and Transformations of the Omicron Phase O in the Ti-Al-Nb System and on the Ambiguity of Its Subvariants O1 and O2. *Scr. Mater.* **2022**, *219*, 114841. https://doi.org/10.1016/j.scriptamat.2022.114841

[17] Shull, R.D.; Cline, J.P. High Temperature X-Ray Diffractometry of Ti-Al Alloys. In *Materials Chemistry at High Temperatures*; Hastie, J.W., Ed.; Humana Press: Totowa, NJ, 1990; pp. 95–117 ISBN 978-1-4612-6781-2.

[18] Chladil, H.F.; Clemens, H.; Leitner, H.; Bartels, A.; Gerling, R.; Schimansky, F.-P.; Kremmer, S. Phase Transformations in High Niobium and Carbon Containing γ-TiAl Based Alloys. *Intermetallics* **2006**, *14*, 1194–1198. https://doi.org/10.1016/j.intermet.2005.11.016

[19] Yeoh, L.A.; Liss, K.-D.; Bartels, A.; Chladil, H.; Avdeev, M.; Clemens, H.; Gerling, R.; Buslaps, T. In Situ High-Energy X-Ray Diffraction Study and Quantitative Phase Analysis in the Alpha plus Gamma Phase Field of Titanium Aluminides. *Scr. Mater.* **2007**, *57*, 1145–1148. https://doi.org/10.1016/j.scriptamat.2007.08.021

[20] Li, X.; Dippenaar, R.; Shiro, A.; Shobu, T.; Higo, Y.; Reid, M.; Suzuki, H.; Akita, K.; Funakoshi, K.-I.; Liss, K.-D. Lattice Parameter Evolution during Heating of Ti-45Al-7.5Nb-0.25/0.5C Alloys under Atmospheric and High Pressures. *Intermetallics* **2018**, *102*, 120–131. https://doi.org/10.1016/j.intermet.2018.08.011

[21] Liss, K.-D.; Funakoshi, K.-I.; Dippenaar, R.J.; Higo, Y.; Shiro, A.; Reid, M.; Suzuki, H.; Shobu, T.; Akita, K. Hydrostatic Compression Behavior and High-Pressure Stabilized β-Phase in γ-Based Titanium Aluminide Intermetallics. *Metals* **2016**, *6*, 165. https://doi.org/10.3390/met6070165

[22] Zhao, W.; Han, J.-K.; Kuzminova, Y.O.; Evlashin, S.A.; Zhilyaev, A.P.; Pesin, A.M.; Jang, J.; Liss, K.-D.; Kawasaki, M. Significance of Grain Refinement on Micro-Mechanical Properties and Structures of Additively-Manufactured CoCrFeNi High-Entropy Alloy. *Mater. Sci. Eng. A* **2021**, *807*, 140898. https://doi.org/10.1016/j.msea.2021.140898

[23] Paul, A.; Liu, X.; Kawasaki, M.; Liss, K.-D. Inverted Magnetic Response in Severe Plastically Deformed Nanostructured High-Entropy Alloy. *Appl. Phys. Lett.* **2023**, *122*, 052402. https://doi.org/10.1063/5.0138040

[24] Kawasaki, M.; Han, J.-K.; Liu, X.; Moon, S.-C.; Liss, K.-D. Synchrotron High-Energy X-Ray & Neutron Diffraction, and Laser-Scanning Confocal Microscopy: In-Situ Characterization Techniques for Bulk Nanocrystalline Metals. *Mater. Trans.* **2023**, *advpub*, MT-MF2022022. https://doi.org/10.2320/matertrans.MT-MF2022022

[25] Yan, K.; Bhattacharyya, D.; Lian, Q.; Kabra, S.; Kawasaki, M.; Carr, D.G.; Callaghan, M.D.; Avdeev, M.; Li, H.; Wang, Y.; et al. Martensitic Phase Transformation and Deformation Behavior of Fe–Mn–C–Al Twinning-Induced Plasticity Steel during High-Pressure Torsion. *Adv. Eng. Mater.* **2014**, *16*, 927–932. https://doi.org/10.1002/adem.201300488

[26] Li, X.; Dippenaar, R.J.; Han, J.-K.; Kawasaki, M.; Liss, K.-D. Phase Transformation and Structure Evolution of a Ti-45Al-7.5Nb Alloy Processed by High-Pressure Torsion. *J. Alloys Compd.* **2019**, *787*, 1149–1157. https://doi.org/10.1016/j.jallcom.2019.02.174

[27] Asta, M.; de Fontaine, D.; van Schilfgaarde, M. First-Principles Study of Phase Stability of Ti–Al Intermetallic Compounds. *J. Mater. Res.* **1993**, *8*, 2554–2568. https://doi.org/10.1557/JMR.1993.2554

[28] Liss, K.-D.; Liu, X.; Li, X.; Han, J.-K.; Dippenaar, R.J.; Kawasaki, M. On the Thermal Evolution of High-Pressure Torsion Processed Titanium Aluminide. *Mater. Lett.* **2021**, *304*, 130650. https://doi.org/10.1016/j.matlet.2021.130650

[29] Kawasaki, M.; Han, H.-K.; Moon, S.-C.; Liss, K.-D. In-Situ Heating Observations on Microstructure Relaxation of Ultrafine-Grained High-Entropy Alloys Using Neutron Diffraction and Laser-Scanning Confocal Microscopy. *Mater. Res. Forum LLC* **2023**.

[30] Liu, X.; Han, J.-K.; Onuki, Y.; Kuzminova, Y.O.; Evlashin, S.A.; Kawasaki, M.; Liss, K.-D. In Situ Neutron Diffraction Investigating Microstructure and Texture Evolution upon Heating of

Nanostructured CoCrFeNi High-Entropy Alloy. *Adv. Eng. Mater.* **2023**, *25*, 2201256. https://doi.org/10.1002/adem.202201256

[31] Nakajima, K.; Kawakita, Y.; Itoh, S.; Abe, J.; Aizawa, K.; Aoki, H.; Endo, H.; Fujita, M.; Funakoshi, K.; Gong, W.; et al. Materials and Life Science Experimental Facility (MLF) at the Japan Proton Accelerator Research Complex II: Neutron Scattering Instruments. *Quantum Beam Sci.* **2017**, *1*, 9. https://doi.org/10.3390/qubs1030009

[32] Liss, K.-D. Materials and Life Science with Quantum Beams at the Japan Proton Accelerator Research Complex. *Quantum Beam Sci.* **2018**, *2*, 10. https://doi.org/10.3390/qubs2020010

[33] Takada, H.; Haga, K.; Teshigawara, M.; Aso, T.; Meigo, S.-I.; Kogawa, H.; Naoe, T.; Wakui, T.; Ooi, M.; Harada, M.; et al. Materials and Life Science Experimental Facility at the Japan Proton Accelerator Research Complex I: Pulsed Spallation Neutron Source. *Quantum Beam Sci.* **2017**, *1*, 8. https://doi.org/10.3390/qubs1020008

[34] Kawasaki, M.; Han, J.-K.; Liu, X.; Onuki, Y.; Kuzminova, Y.O.; Evlashin, S.A.; Pesin, A.M.; Zhilyaev, A.P.; Liss, K.-D. In Situ Heating Neutron and X-Ray Diffraction Analyses for Revealing Structural Evolution during Postprinting Treatments of Additive-Manufactured 316L Stainless Steel. *Adv. Eng. Mater.* **2022**, *24*, 2100968. https://doi.org/10.1002/adem.202100968

[35] Liss, K.-D.; Bartels, A.; Clemens, H.; Bystrzanowski, S.; Stark, A.; Buslaps, T.; Schimansky, F.-P.; Gerling, R.; Scheu, C.; Schreyer, A. Recrystallization and Phase Transitions in a Gamma-TiAl-Based Alloy as Observed by Ex Situ and in Situ High-Energy X-Ray Diffraction. *Acta Mater.* **2006**, *54*, 3721–3735. https://doi.org/10.1016/j.actamat.2006.04.004

[36] Yan, K.; Liss, K.-D.; Garbe, U.; Daniels, J.; Kirstein, O.; Li, H.; Dippenaar, R. From Single Grains to Texture. *Adv. Eng. Mater.* **2009**, *11*, 771–773. https://doi.org/10.1002/adem.200900163

[37] Liss, K.-D.; Garbe, U.; Li, H.; Schambron, T.; Almer, J.D.; Yan, K. In Situ Observation of Dynamic Recrystallization in the Bulk of Zirconium Alloy. *Adv. Eng. Mater.* **2009**, *11*, 637–640. https://doi.org/10.1002/adem.200900094

[38] Liss, K.-D.; Yan, K. Thermo-Mechanical Processing in a Synchrotron Beam. *Mater. Sci. Eng. - Struct. Mater. Prop. Microstruct. Process.* **2010**, *528*, 11–27. https://doi.org/10.1016/j.msea.2010.06.017

[39] Liss, K.-D.; Schmoelzer, T.; Yan, K.; Reid, M.; Peel, M.; Dippenaar, R.; Clemens, H. In Situ Study of Dynamic Recrystallization and Hot Deformation Behavior of a Multiphase Titanium Aluminide Alloy. *J. Appl. Phys.* **2009**, *106*, 113526-113526–6. https://doi.org/doi:10.1063/1.3266177

[40] Liss, K.-D. Thermo-Mechanical Processing in a Synchrotron Beam - from Simple Metals to Multiphase Alloys and Intermetallics. *World J. Eng.* **2010**, *7*, P438,1-4.

[41] Liss, K.D. Thermo-Mechanical Processing in a Synchrotron Beam. *Mater. Sci. Forum* **2012**, *715–716*, 102–102. https://doi.org/10.4028/www.scientific.net/MSF.715-716.102